JGR Oceans

RESEARCH ARTICLE
10.1029/2024JC021174

Special Collection:
Science from the Surface Water and Ocean Topography Satellite Mission

Internal Tides From SWOT: A 75-Day Instantaneous Mode-1 M_2 Internal Tide Model

Zhongxiang Zhao[1,2]

[1]Applied Physics Laboratory, University of Washington, Seattle, WA, USA, [2]School of Oceanography, University of Washington, Seattle, WA, USA

Key Points:

- Models SWOT-75d and Nadir-30y are constructed using 75 days of SWOT data and 30 years of nadir altimetry data in 1993–2022, respectively
- Comparison and evaluation of SWOT-75d and Nadir-30y reveal that mode-1 M_2 internal tides are subject to significant temporal variations
- Phase anomalies of SWOT-75d with respect to Nadir-30y are used to improve internal tide correction for SWOT

Correspondence to:
Z. Zhao,
zzhao@uw.edu

Citation:
Zhao, Z. (2024). Internal tides from SWOT: A 75-day instantaneous mode-1 M_2 internal tide model. *Journal of Geophysical Research: Oceans*, *129*, e2024JC021174. https://doi.org/10.1029/2024JC021174

Received 3 APR 2024
Accepted 20 NOV 2024

Author Contribution:
Conceptualization: Zhongxiang Zhao
Data curation: Zhongxiang Zhao
Methodology: Zhongxiang Zhao
Software: Zhongxiang Zhao
Writing – original draft: Zhongxiang Zhao
Writing – review & editing: Zhongxiang Zhao

Abstract Seventy-five days of sea surface height measurements made by the Surface Water and Ocean Topography (SWOT) mission from 7 September to 21 November 2023 are used to explore SWOT's capability of observing internal tides. Mode-1 M_2 internal tides are mapped by our updated mapping technique. SWOT-75d represents a 75-day instantaneous model. Nadir-30y is constructed using 30 years of nadir altimetry data from 1993 to 2022 and represents a climate normal. The nadir altimetry data in 2023 are used for model evaluation. Despite its large errors, SWOT-75d reveals the basic features of the global mode-1 M_2 internal tide field, and causes positive variance reduction in regions of strong internal tides. Nadir-30y performs better overall, but SWOT-75d performs better in the tropical South Atlantic Ocean, the central North Pacific Ocean, and the Melanesian region. Evaluation using seasonally subsetted altimetry data reveals that M_2 internal tides have significant temporal variations. SWOT-75d performs the best in fall, because the model is constructed using data largely in fall. SWOT-75d has large phase anomalies, which are spatially smoothed and used to adjust the phases in Nadir-30y. The phase-adjusted model can better make internal tide correction for SWOT and its performance is improved by 20%. Our results demonstrate that (a) mode-1 M_2 internal tides can be extracted from 75 days of SWOT data by our mapping technique, and (b) the instantaneous internal tide model can be used to improve internal tide correction for SWOT.

Plain Language Summary Internal tides are ubiquitous in the global ocean and have drawn great research interest in recent years. Our knowledge of internal tides has been greatly improved, thanks to more than 30 years of SSH measurements made by multiple nadir altimetry missions. However, our capability of observing internal tides is severely limited by the one-dimensional SSH from nadir-looking altimetry missions. The new wide-swath SWOT mission measures two-dimensional SSH along a 120-km swath with a spatial resolution of 2 km. We explore SWOT's capability of observing internal tides using the recently released 75 days of SWOT data from 7 September to 21 November 2023. We demonstrate that we can extract mode-1 M_2 internal tides from such a short data record by our mapping technique. The SWOT-derived model performs better than a 30-year coherent model in some regions. Its phase information can be used to improve internal tide correction for SWOT. Our work demonstrates that SWOT greatly improves our capability of observing internal tides.

1. Introduction

Internal tides are ubiquitous in the global ocean and have distinguished periodic signatures in field and satellite measurements (Alford, 2003; MacKinnon et al., 2017; Whalen et al., 2020). Internal tides originate in the interaction of barotropic tides and topographic features and propagate over hundreds to thousands of km in the open ocean (Arbic, 2022; Egbert & Ray, 2000; Garrett & Kunze, 2007; Zhao et al., 2016). Internal tides have drawn great research interest in recent years, because they play an important role in a variety of ocean processes such as tracer transport, primary productivity, and upper ocean mixing (Masunaga et al., 2020; Ray & Susanto, 2016; Spingys et al., 2020; Storlazzi et al., 2020; Susanto & Ray, 2022; Tuerena et al., 2019; Zaron et al., 2023; Zhang et al., 2021). The magnitude and geography of internal tide driven mixing affect meridional overturning circulation and global climate (Jayne & St. Laurent, 2001; Melet et al., 2016; Munk & Wunsch, 1998). The generation and propagation of internal tides are strongly modulated by ever-changing stratification and ocean circulation; therefore, internal tides are subject to significant temporal variations from days to decades (Kelly et al., 2016; Nash et al., 2012; Zaron & Egbert, 2014; Zhao, 2023b). A fraction of internal tides loses phase locking with barotropic tidal forcing and becomes incoherent internal tides. Taking advantage of their temporal variability, long-range internal tides can be used to monitor the ocean interior structure via

propagation speed (Zhao, 2016). On the other hand, internal tides are unwanted signals that should be accurately corrected to study submesoscale motions (Morrow et al., 2019; Soares et al., 2022; Torres et al., 2018). However, it is challenging to correct incoherent internal tides using traditional internal tide models with time-invariable harmonic constants. One long-standing and pressing task in the oceanographic community is to improve our capability of observing internal tides on a global scale.

Our knowledge of internal tides has been significantly improved by satellite altimetry observations (Ray & Mitchum, 1996, 1997). Several observational internal tide models have been constructed using nadir altimetry data collected in the past years (Ray & Zaron, 2016; Ubelmann et al., 2022; Zaron, 2019; Zaron & Elipot, 2024; Zhao et al., 2016). All these models are based on multiyear altimetry data and thus contain only the phase-locked coherent (stationary) internal tides, missing incoherent internal tides caused by their temporal variations. The continuous operation of multiple nadir altimetry missions from 1993 to 2022 yielded a data record about 120 satellite years long. The long data record can significantly suppress errors and thus improve internal tide models. For example, our latest mode-1 M_2 internal tide model is constructed using 30 years of nadir altimetry data from 1993 to 2022 (Zhao, 2023a). It is a 30-year coherent model and labeled Nadir-30y in this study. The 120-year data record can be divided into small subsets to study the seasonal and interannual variations of internal tides (Zhao, 2021, 2023b). However, the along-track one-dimensional SSH data from nadir-looking altimetry have wide inter-track intervals, which severely affect our capability of observing internal tides. In previous studies, we have not attempted to map instantaneous internal tide fields in time windows shorter than 3 months.

The new SWOT mission measures two-dimensional SSH along a 120-km swath with a 20-km nadir gap (Fu et al., 2024; Morrow et al., 2019). SWOT has a long repeat cycle of 21 days, which makes it difficult to extract high-frequency internal tides. In January 2024, the SWOT project published 75 days of SWOT science data from 7 September to 21 November 2023 (SWOT Project, 2024). The data are along its 21-day repeat orbit with 584 swaths globally. We are motivated to analyze the 75 days of SWOT data using our updated mapping technique. In the past years, we have developed a mapping procedure that consists of two rounds of plane wave analysis with spatial bandpass filtering in between, and applied it to study the temporal variations of internal tides (Zhao, 2022a, 2022b, 2023a, 2023b). Our technique is computationally intensive, but it significantly suppresses model errors by multiple rounds of spatial and temporal filtering. In this paper, we explore SWOT's capability of observing internal tides using the 75 days of SWOT data. We will address the following two questions:

1. *Can we extract mode-1 M_2 internal tides using the 75 days of SWOT data?* We map mode-1 M_2 internal tides using the 75 days of SWOT data by our updated mapping technique. We obtain an internal tide model labeled SWOT-75d. Evaluation using independent altimetry data shows that SWOT-75d reduces variance in regions of strong internal tides and even reduces more variance than Nadir-30y in regions such as the central North Pacific Ocean. The results show that we can extract mode-1 M_2 internal tides from the 75 days of SWOT data by our mapping technique.
2. *Can we improve internal tide correction for SWOT?* SWOT-75d represents a 75-day instantaneous internal tide model in September–November 2023. Nadir-30y represents a climate normal averaged over three decades from 1993 to 2022. We find that SWOT-75d has large phase anomalies with respect to Nadir-30y, mainly caused by seasonal and interannual variability. We adjust the phases in Nadir-30y using the spatially smoothed phase anomalies of SWOT-75d. The phase-adjusted model performs better in making internal tide correction for SWOT. The results show that we can partially correct time-varying internal tides caused by seasonal and interannual variability.

The rest of this paper is arranged as follows. Section 2 describes the satellite altimetry data. Section 3 briefly describes our latest three-step mapping procedure. In Section 4, we compare and evaluate the two internal tide models. In Section 5, we show the improvement of internal tide correction utilizing the instantaneous internal tide model. Section 6 discusses the impact of the SWOT data along its 1-day repeat orbit. Section 7 contains a summary and perspectives.

2. Satellite Altimetry Data

2.1. SWOT Altimetry Data

The SWOT mission was launched in December 2022 (Fu et al., 2024; Qiu et al., 2024). SWOT measures the two-dimensional SSH field using a Ka-band Radar Interferometer (KaRIn) (Rodriguez et al., 2017, & references

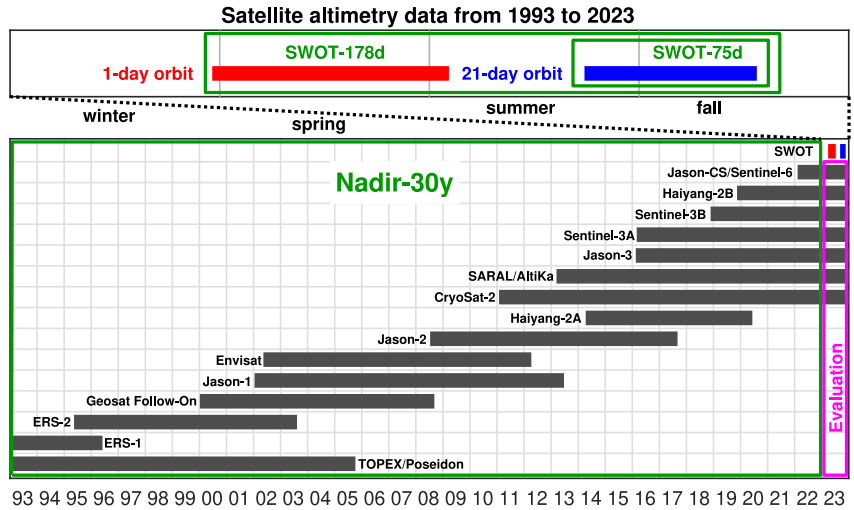

Figure 1. Satellite altimetry data from 1993 to 2023. Nadir-30y represents a climate normal of mode-1 M_2 internal tides constructed using 30 years of nadir altimetry data from 1993 to 2022. SWOT-75d gives an instantaneous model constructed using 75 days of SWOT data from 7 September to 21 November 2023. SWOT-178d is constructed using 178 days of SWOT data along both the 21-day and 1-day orbits.

therein). KaRIn measures SSH using phase lags of Ka-band radar waves. In contrast, the Jason-class nadir altimeter measures SSH using travel times of Ku-band radar waves. Therefore, KaRIn's instrumental errors are about one order of magnitude lower (Fu et al., 2024). SWOT measures SSH along a 120-km swath with a 2-km spatial resolution (Wang et al., 2019). In its calibration phase in 2023, SWOT occupied a 1-day repeat orbit with 28 swaths globally. In its science phase since July 2023, SWOT occupies a 21-day repeat orbit with 584 swaths globally. The number of SSH observations at one given site in one 21-day science cycle is a function of latitude, ranging from 1 at low latitudes to 20 at high latitudes. In January 2024, the SWOT project published some SWOT data to the scientific community, including two sets of low-rate SSH measurements in the open ocean (SWOT Project, 2024). The first data set is about 103 days long from 29 March to 10 July 2023 in its 1-day calibration orbit (Figure 1, red). The second data set is about 75 days long from 7 September to 21 November 2023 along its 21-day science orbit (Figure 1, blue).

One of SWOT's main scientific goals is detecting submesoscale motions (Durand et al., 2010; Fu & Ferrari, 2008; Morrow et al., 2019). Fortunately, SWOT also offers a great opportunity for mapping internal tides, thanks to its wide swath, high spatial resolution, and low model errors. Our primary goal in this study is to explore whether or not we can map mode-1 M_2 internal tides using 75 days of SWOT data. The SWOT data have been processed for a wide variety of error sources such as wet troposphere and significant wave height (Dibarboure et al., 2022). Among them, internal tides have been corrected using an observational model developed by Zaron (2019). The model is a multiyear coherent (stationary) model, missing the incoherent (non-stationary) internal tide component. In this study, we add the modeled internal tide signals back to the SWOT data, because we will map mode-1 M_2 internal tides, instead of their residuals. We aim to construct a mode-1 M_2 internal tide model using 75 days of science data that cover the global ocean with 584 swaths (Figure 2a, black). Our mapping procedure is described in Section 3. The model is labeled SWOT-75d, because it represents a 75-day internal tide model. However, the 103 days of 1-day calibration data are along 28 swaths only (Figure 2a, red). We cannot map mode-1 M_2 internal tides using the 1-day repeat data alone. In Section 6, we will map mode-1 M_2 internal tides using the combined 1-day and 21-day repeat data, and discuss the impact of the 1-day repeat data. Figure 2b shows the number of SSH data per 160 km by 160 km fitting window for SWOT-75d. There are usually more than 3×10^4 data in each window. Figure 2c shows the number of SSH data per 160 km by 160 km fitting window for SWOT-178d. It shows much higher data density along the 1-day orbit (red stripes).

2.2. Nadir Altimetry Data

In an earlier study, we have constructed a mode-1 M_2 internal tide model using 30 years of SSH measurements from 1993 to 2022 following the same mapping procedure (Section 3). The measurements are made by 15 nadir

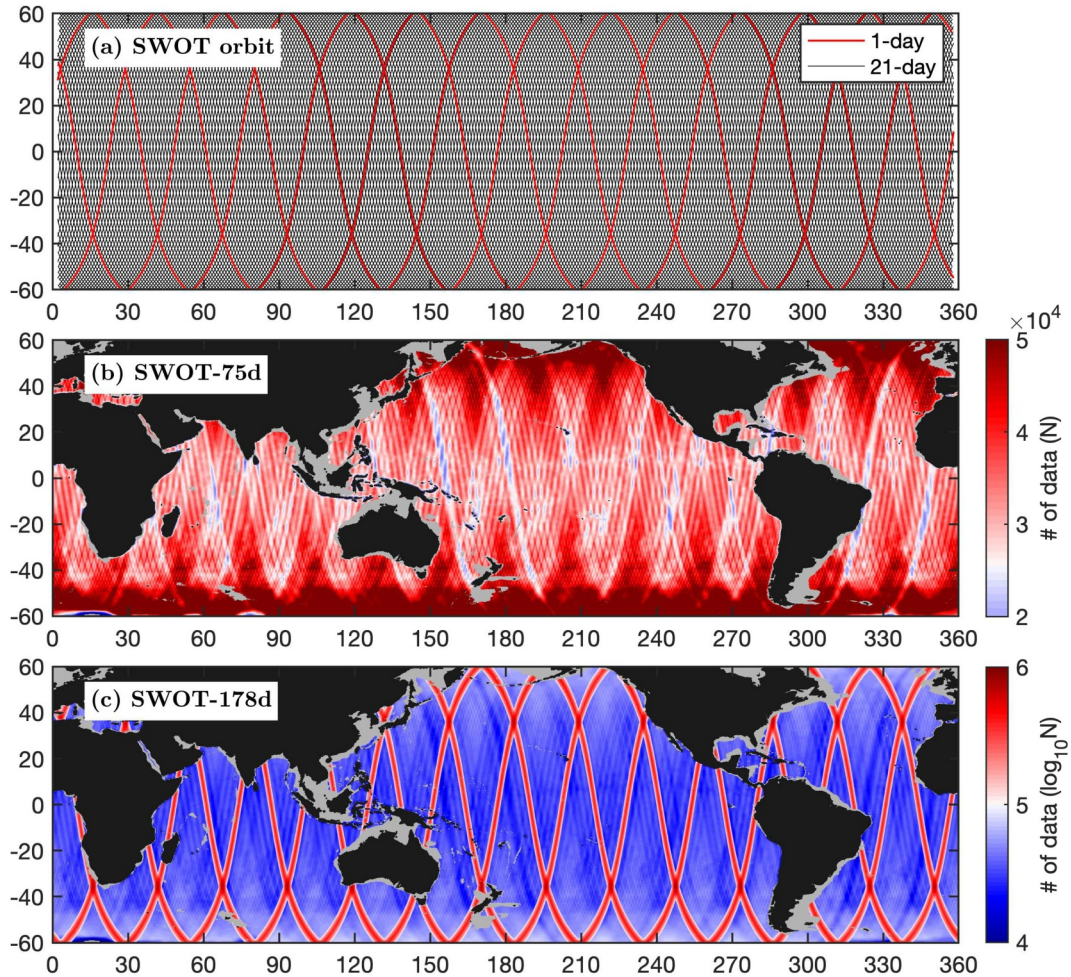

Figure 2. Global distribution of SWOT data in 2023. (a) SWOT orbits. The 1-day and 21-day orbits have 28 and 586 swaths, respectively. (b) Number of SSH data (in linear scale) per 160 km by 160 km window for SWOT-75d. (c) Number of SSH data (in logarithmic scale) per 160 km by 160 km for SWOT-178d.

altimetry missions (Figure 1). The data used in this paper are the along-track SSH measurements distributed by the Copernicus Marine Service (https://doi.org/10.48670/moi-00146). The SSH measurements have been processed by standard corrections for atmospheric effects, surface wave biases, geophysical effects, ocean barotropic tide, and solid Earth tide (Pujol et al., 2016; Taburet et al., 2019). The model is labeled Nadir-30y, which represents the 30-year coherent model from 1993 to 2022.

The nadir altimetry data in 2023 are not used to construct SWOT-75d or Nadir-30y. They are independent data and will be used to evaluate the newly developed internal tide models. The SSH measurements are made by seven concurrent nadir altimetry missions: SARAL/AltiKa, CryoSat-2, Haiyang-2B, Jason-3, Sentinel-3A, Sentinel-3B, and Sentinel-6 (Figure 1). The nadir altimetry data in 2023 are also distributed by the Copernicus Marine Service.

3. Methods

3.1. Plane Wave Analysis

Plane wave analysis is our core technique of mapping internal tides from satellite altimetry. This technique has been constantly improved in a series of studies (Zhao, 2020; Zhao & Alford, 2009; Zhao et al., 2016). Plane wave analysis maps internal tides using satellite SSH measurements in a fitting window, which is empirically chosen to be 160 km by 160 km, consistent with the wavelengths of mode-1 M_2 internal tides (Zhao, 2022b). Each fitting window contains a large number of SSH data (Figure 2), so that plane wave analysis can significantly reduce

model errors. The target internal tidal wave $\eta\ (A,\ \phi,\ \theta)$ has three parameters to be determined: amplitude A, phase ϕ, and propagation direction θ. There are multiple mode-1 M_2 internal waves in arbitrary propagation directions at one site. Five internal tidal waves at each given site are sufficient to describe the multi-wave internal tide field (Zhao, 2022b). The target internal tidal waves follow

$$\sum_{m=1}^{5} A_m \cos\left(\omega\, t + \phi_m - k\, x \cos\theta_m - k\, y \sin\theta_m\right), \tag{1}$$

where x and y are the east and north Cartesian coordinates, t is time, ω and k are the frequency and wavenumber of mode-1 M_2 internal tides, respectively. The wavenumber is a function of location, and computed by solving the Sturm-Liouville problem using the World Ocean Atlas 2018 (WOA18) climatological hydrography (Boyer et al., 2018; Kelly, 2016; Zhao et al., 2016). The resulting wavelengths (phase speeds) of mode-1 M_2 internal tides have been previously shown in Figure 1 of Zhao (2021). Using SSH data in one given fitting window, the amplitude A, phase ϕ, and propagation direction θ of one target internal tidal wave are determined by least-squares fits. In each compass direction (increment 1°), the amplitude and phase of one plane wave are determined. When the resulting amplitudes are plotted as a function of direction in polar coordinates, an internal tidal wave appears to be a lobe. The amplitude and direction of the first wave are determined from the largest lobe. After determining one wave, its signal is predicted and subtracted from the original data. An iterative algorithm has been developed to extract five internal waves one by one. The vector sum of the five waves gives the internal tide solution at the given grid point.

3.2. Spatial Bandpass Filtering

Plane wave analysis allows us to construct the mode-1 M_2 internal tide field at a regular grid (0.2° longitude by 0.2° latitude) from satellite along-track SSH data. Taking advantage of the horizontally regular field, M_2 internal tides can be further filtered by removing nontidal components constrained by the wavenumber requirement. The M_2 internal tide field is converted to a two-dimensional (2-D) wavenumber spectrum by Fourier transform in overlapping 850 by 850 km windows. The 2-D wavenumber spectrum reveals that the variance is mainly around the theoretical wavenumber (Zhao, 2020). The variance falling outside the theoretical wavenumber range is due to nontidal errors. The 2-D spectrum is truncated to (0.9, 1.2) times the local wavenumber (Appendix A). Then the truncated spectrum is converted back to the internal tide field by inverse Fourier transform. The cutoff wavenumbers are empirically determined. They reflect the spectral peaks of M_2 internal tides determined by the length of the data record. Note that Nadir-30y is constructed using cutoff wavenumbers of (0.8, 1.25) times the local wavenumber (Zhao, 2023a).

3.3. Three-Step Mapping Procedure

Our 3-step mapping procedure comprises two rounds of plane wave analysis with a spatial bandpass filter in between (Zhao, 2022a, 2022b). In the first step, mode-1 M_2 internal tides are mapped at a spatially regular grid by plane wave analysis from satellite data along discrete ground tracks (Section 3.1). The M_2 internal tides are at a regular grid of 0.2° longitude by 0.2° latitude. In the second step, the horizontally regular M_2 internal tide field is cleaned by spatial bandpass filtering (Section 3.2). The 2-D filtered internal tide field is a multi-wave summed interference field. In the third step, plane wave analysis is called again to decompose the filtered internal tide field into five internal waves at each grid point. The second-round plane wave analysis is the same as the first round, except that the input is the filtered internal tide field in the second step. In the end, there are 5 mode-1 M_2 internal waves at each grid point. The same mapping procedure is employed to map SWOT-75d and Nadir-30y. The 3-step mapping procedure has been described in our previous papers. To avoid repetition, an interested reader is referred to Zhao (2022a, 2022b) for more details.

4. Comparison of SWOT-75d and Nadir-30y

4.1. Spatial Features

SWOT-75d and Nadir-30y are shown in Figure 3 for direct comparison. It is obvious that SWOT-75d is poor in comparison with the 30-year-coherent Nadir-30y. This is reasonable. Although the 75 days of SWOT data are long enough to separate M_2 from S_2 and N_2 constituents (Appendix C), SWOT-75d has a wide M_2 spectral peak

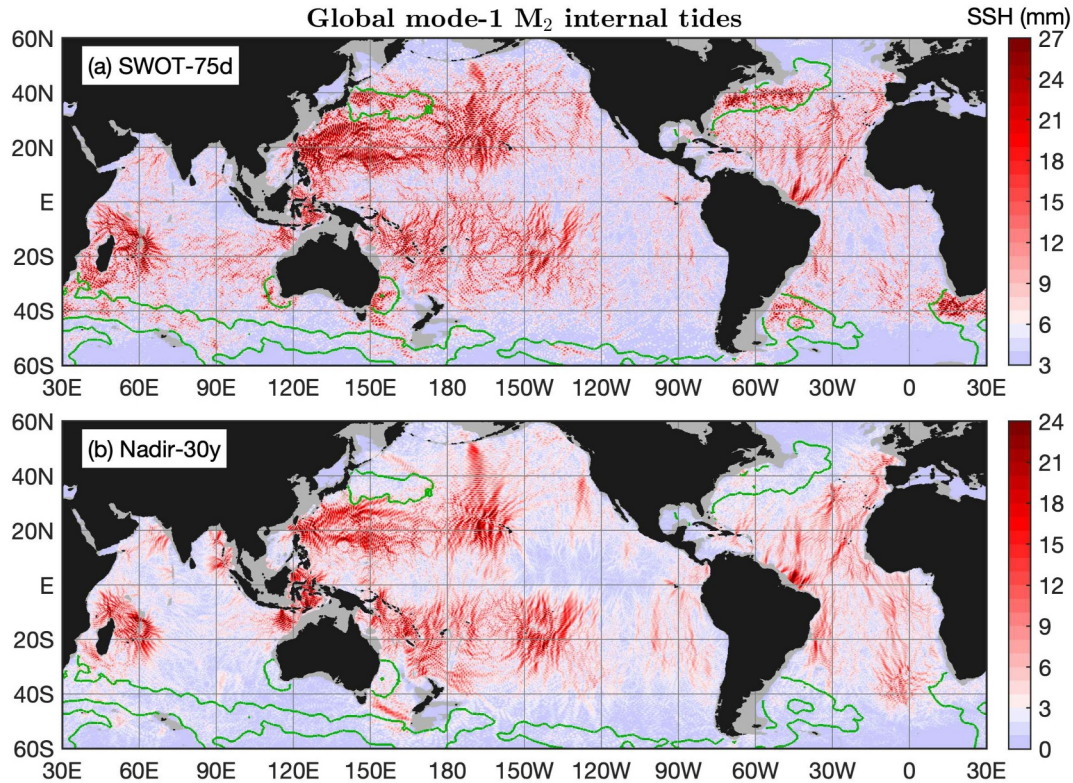

Figure 3. Global mode-1 M_2 internal tides. (a) SWOT-75d. (b) Nadir-30y. The two models have similar spatial patterns, with a correlation coefficient of 0.63. Their color maps are shifted by 3 mm for better contrast of signals and errors. Green contours indicate high EKE regions, where both internal tide models are not reliable.

in the frequency domain and thus contains large errors leaked from mesoscale eddies. In contrast, the 30 years of nadir altimetry data from 1993 to 2022 are sufficiently long, so that Nadir-30y has a narrow M_2 spectral peak and thus contains small errors (Zhao, 2023a). The time windows of SWOT-75d and Nadir-30y are 75 days and 30 years, respectively, with a ratio of 1: 150. Therefore, Nadir-30y gives a climate normal of mode-1 M_2 internal tides, while SWOT-75d gives a 75-day instantaneous internal tide model. Despite its large errors, SWOT-75d reveals the basic features of the global mode-1 M_2 internal tide field. For example, energetic internal tides are observed around the Hawaiian Ridge, around the French Polynesian Ridge, in the western North Pacific Ocean, and in the Madagascar-Mascarene region. SWOT-75d also reveals well-defined long-range internal tidal beams in the Atlantic Ocean, in the Arabian Sea, southward from the Mendocino Ridge, in the Tasman Sea, and northward from the French Polynesian Ridge. SWOT-75d and Nadir-30y are overall spatially similar, with a correlation coefficient of 0.63. In terms of SSH amplitude, SWOT-75d is greater than Nadir-30y by 70%, due mainly to model errors (Figure 4).

4.2. Model Errors

We have developed an objective method for estimating model errors by background internal tides (Zhao, 2023a, 2023b). Background internal tides are mapped using the same altimetry data following the same mapping procedure but for a slightly different tidal period (Appendix C). In this study, we choose a tidal period of 12.3373 hr (M_2 minus 5 min). There are no major tidal constituents at this period; therefore, the plane-wave fitted signals are mostly errors that are determined by the input altimetry data and the mapping technique. A similar strategy has been employed previously to estimate barotropic tide errors (Ray & Susanto, 2016; Zaron et al., 2023). The resulting model errors in SWOT-75d and Nadir-30y are shown in Figure 4. For both models, large errors are mainly in regions of high eddy Kinetic energy (EKE) (Figure 4, green contours), because model errors are mainly leaked mesoscale signals. The area-weighted mean errors in SWOT-75d and Nadir-30y are 5 and 0.7 mm, respectively. Nadir-30y has much lower model errors, due to its 120 satellite years of data. SWOT-75d has large

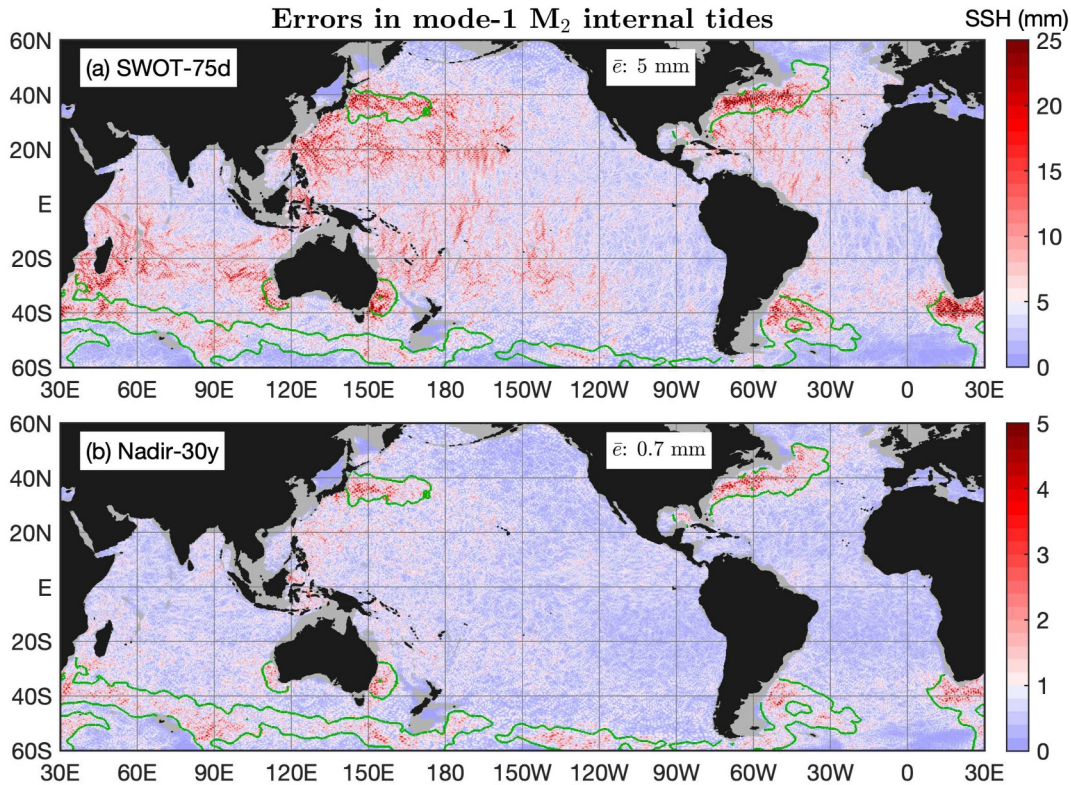

Figure 4. Model errors estimated using mode-1 M_2 internal tides mapped using the same altimetry data following the same mapping procedure but for a tidal period of M_2 minus 5 min (a) SWOT-75d. (b) Nadir-30y. Green contours indicate high EKE regions. Global mean errors are given.

errors in regions of strong internal tides (e.g., the Hawaiian Ridge and the French Polynesian Ridge), because of its short data record and wide M_2 spectral peak (Appendix C). Note that the two models are constructed using slightly different bandpass widths (Appendix A). Therefore, it is meaningless to compare their amplitude and energetics, which are overwhelmed by model errors.

4.3. Evaluation Using Independent Altimetry Data

SWOT-75d and Nadir-30y are evaluated using the full-year independent nadir altimetry data in 2023 (Figure 1, magenta box). The evaluation method has been widely employed in previous studies (Ray & Zaron, 2016; Zaron, 2019; Zhao, 2021). For each SSH measurement of known time and location, the internal tide signal is predicted using the model under evaluation and subtracted from the original data. The variance reduction is the variance difference before and after the internal tide correction. In the end, the variance reductions from all SSH measurements are averaged in 1° by 1° bins.

Figure 5 gives variance reductions explained by SWOT-75d and Nadir-30y. Figure 5a shows that SWOT-75d can reduce variance in regions of strong internal tides such as the Hawaiian Ridge, the French Polynesian Ridge, the western North Pacific, the Amazon shelf, and the Mendocino Ridge (red patches). This is understandable, because strong internal tides can overcome large model errors in SWOT-75d. However, negative variance reductions occur in regions of weak internal tides such as the tropical Pacific Ocean, the South Pacific Ocean, and the central and southern Indian Ocean, where model errors may be larger than internal tides. Note that both SWOT-75d and Nadir-30y cause negative variance reductions in high EKE regions (gray), where the satellite observed internal tides are not reliable. Its area-weighted mean variance reduction is 5.7 mm^2. The performance of SWOT-75d in correcting internal tides is encouraging, considering that SWOT-75d has large model errors (Figure 4a). The evaluation reveals that SWOT-75d contains useful information, despite its large errors.

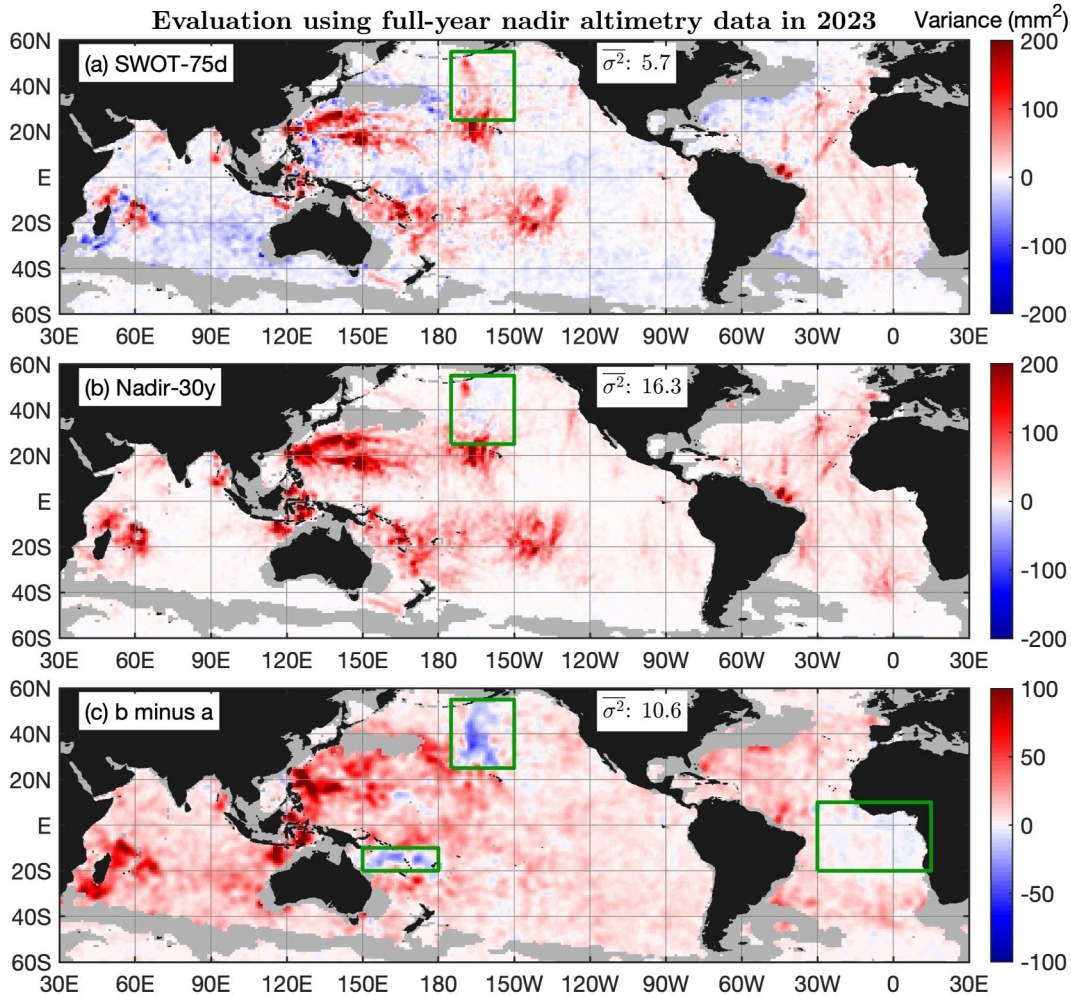

Figure 5. Evaluation of SWOT-75d and Nadir-30y using the full-year nadir altimetry data in 2023. Shown are variance reductions obtained by making internal tide correction. High EKE regions are masked. (a) SWOT-75d. (b) Nadir-30y. (c) b minus a. SWOT-75d performs better than Nadir-30y in the tropical South Atlantic Ocean, the central North Pacific Ocean, and the Melanesian region (green boxes).

Figure 5b shows that Nadir-30y causes positive variance reductions throughout the global ocean, due to its small model errors (Figure 4b). Its area-weighted mean variance reduction is 16.3 mm^2. It suggests that Nadir-30 is a reliable model for internal tide correction. To better compare SWOT-75d and Nadir-30y, we calculate and show their differences in Figure 5c. The overall positive differences suggest that Nadir-30y performs better than SWOT-75d throughout the global ocean, except for three remarkable exceptions (green boxes): the tropical South Atlantic Ocean, the central North Pacific Ocean, and the Melanesian region. It is worth pointing out that SWOT-75d performs better than Nadir-30y in three regions, which suggests that SWOT-75d may be helpful in internal tide correction. We suggest that the phases of M_2 internal tides in the three regions have large changes in the past 30 years with global ocean warming, so that the phases in Nadir-30y (averaged over 30 years) cannot accurately reflect the instantaneous phases in 2023 (Appendix B). In contrast, SWOT-75 contains important instantaneous phases in 2023 and thus performs better. This feature will be further explored in the next two sections. In summary, the evaluation using independent altimetry data in 2023 suggests that SWOT-75d has its admirable advantages, despite its large errors and overall poor performance.

4.4. Model Evaluation Using Seasonal Subsets

We next evaluate SWOT-75d and Nadir-30y using four seasonal subsets (winter, spring, summer, and fall) of the nadir altimetry data in 2023 (Figure 1). SWOT-75d is constructed using SWOT data from 7 September to

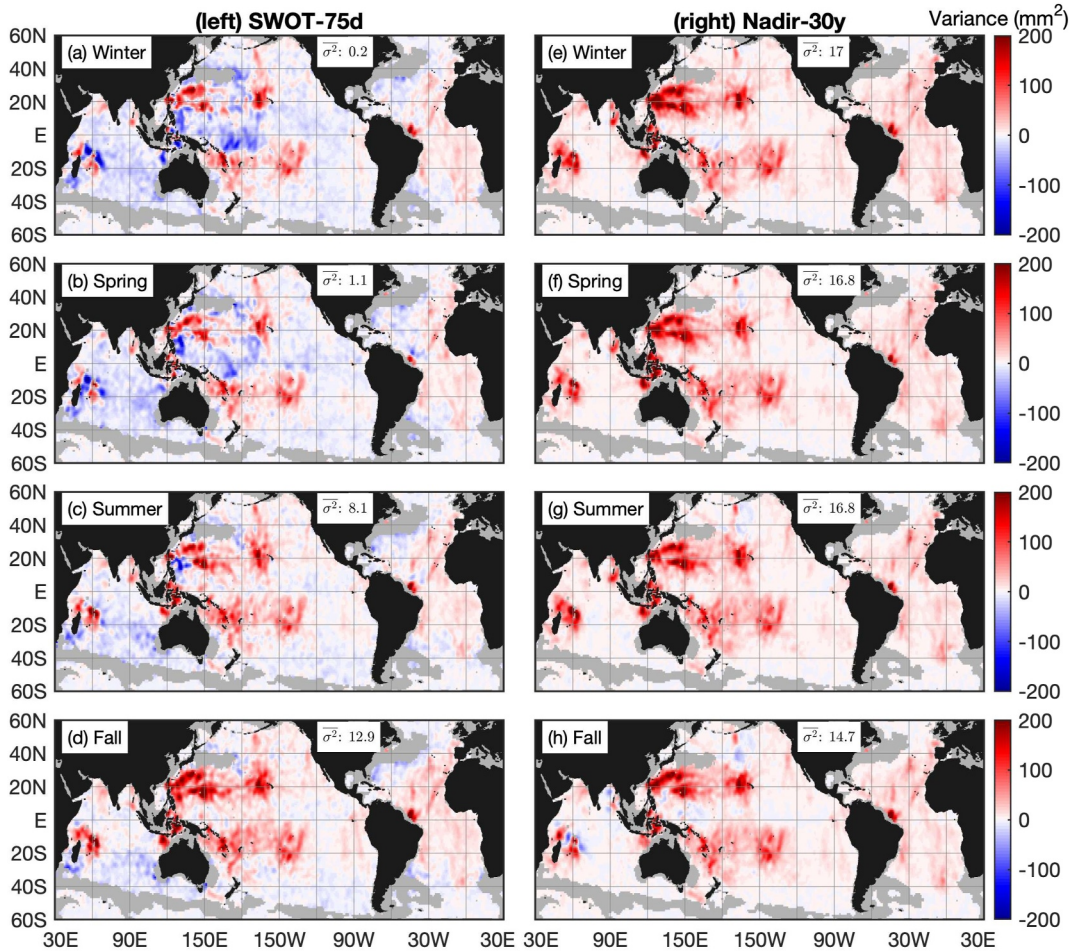

Figure 6. Evaluation of SWOT-75d (left) and Nadir-30y (right) using four seasonal subsets of the nadir altimetry data in 2023. Shown are variance reductions obtained by making internal tide correction. High EKE regions are masked. (a, e) Winter (JFM). (b, f) Spring (AMJ). (c, g) Summer (JAS). (d, h) Fall (OND). Global area-weighted mean values are given.

November 21, which are generally in fall (Figure 1). SWOT-75d thus represents the M_2 internal tide model in fall. On the contrary, Nadir-30y is constructed using 30 years of nadir altimetry data, without significant seasonal bias. Therefore, we hypothesize that their performance in internal tide correction is affected by the seasonality of the independent altimetry data. This analysis is motivated by our observation of seasonal mode-1 M_2 internal tides (Appendix B). We observe large phase anomalies in the tropical zone, which may affect SWOT-75d's performance in correcting internal tides.

Figure 6 shows the seasonal variance reductions caused by SWOT-75d and Nadir-30y. The evaluation method is the same as described in Section 4.3. We also calculate area-weighted mean variance reductions. We find that the performance of SWOT-75d has a strong seasonal cycle, with its variance reductions ranging from 0.2 mm^2 in winter to 12.9 mm^2 in fall. It is reasonable that SWOT-75d performs the best in fall, because the model itself is constructed using SWOT data largely in fall (Figure 1). It is worth pointing out that SWOT-75d can cause positive variance reductions in all four seasons in regions of strong internal tides. The result is consistent with the large seasonal phase anomalies of mode-1 M_2 internal tides discussed in Appendix B. Figure 6 also shows that the seasonal variance reduction by Nadir-30y ranges from 14.7 mm^2 in fall to 17 mm^2 in winter. The slight seasonal differences are likely caused by the unequal distribution of internal tides in the southern and northern hemispheres.

We next examine the performance of SWOT-75d and Nadir-30y in the four seasons. Figure 7 shows their seasonal variance reduction differences. The area-weighted mean values are always positive, suggesting that Nadir-30y

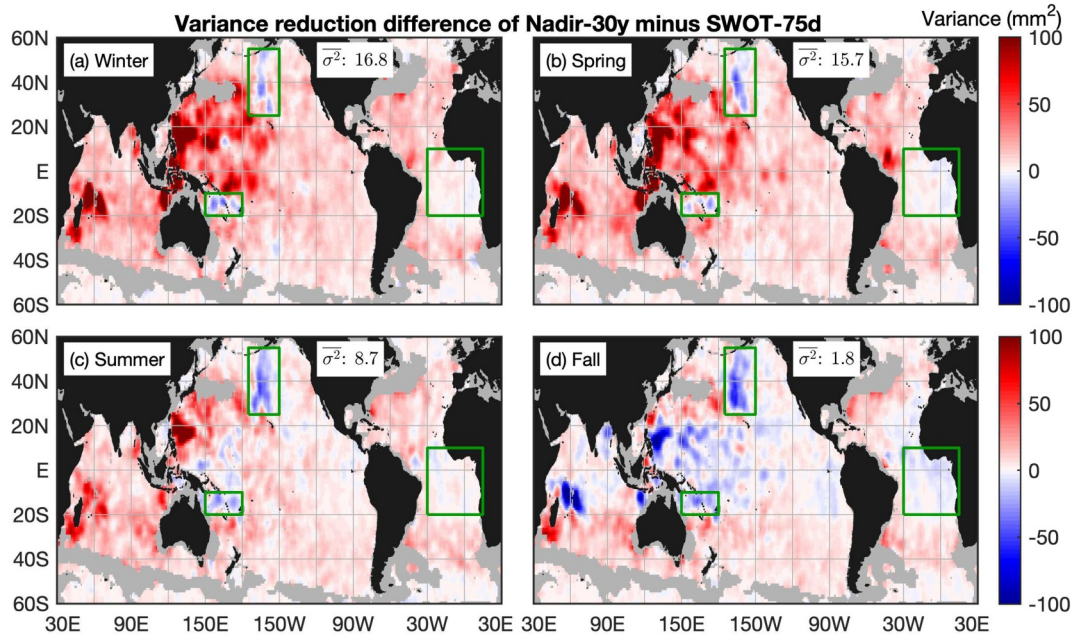

Figure 7. Variance reduction differences of Nadir-30y minus SWOT-75d. In (a–c), Nadir-30y performs better than SWOT-75d overall except for the tropical South Atlantic Ocean, the central North Pacific Ocean, and the Melanesian region (green boxes). In (d), SWOT-75d is better than Nadir-30y also in the tropical zone within 20°S/N. High EKE regions are masked. Global area-weighted mean values are given.

performs better than SWOT-75d throughout the year. We find two interesting features. First, SWOT-75d always performs better than Nadir-30y in three regions (green boxes): the tropical South Atlantic Ocean, the central North Pacific Ocean, and the Melanesian region. Second, SWOT-75d performs better than Nadir-30y in the tropical zone (±20°) in fall (Figure 7d). SWOT-75d is constructed using SWOT data largely in fall; thus it is reasonable that it performs the best in fall. In addition, the seasonal differences are mainly in the tropical zone, because the seasonal phase variations of internal tides are strongest in the tropical zone (Appendix B). For the same reason, SWOT-75d does a better job than Nadir-30 in the tropical zone in fall. All these features suggest that M_2 internal tides are subject to significant seasonal variations. For internal tide models constructed using data records shorter than 1 year, their performance in correcting internal tides is affected by the seasonality of internal tides. Therefore, the seasonal cycle should be taken into account in correcting internal tides for SWOT.

5. Improving Internal Tide Correction for SWOT

It is well known that previous multiyear coherent internal tide models cannot correct time-varying internal tides (Carrere et al., 2021). It is a challenging task to correct incoherent internal tides for SWOT. Fortunately, we construct a 75-day instantaneous internal tide model using wide-swath SWOT data and show that SWOT-75d performs better than Nadir-30y in some regions, thanks to its instantaneous phases. Based on this advance, we bring up a new method of improving internal tide correction for SWOT taking advantage of the instantaneous phases of SWOT-75d.

5.1. Phase Anomalies of SWOT-75d

We first examine the phase anomalies of SWOT-75d with respect to the climate normal Nadir-30y. Because SWOT-75d is an instantaneous internal tide model, its phase anomalies reflect the instantaneous phases of M_2 internal tides during the 75-day time window. In this study, positive (negative) phase anomalies indicate that SWOT-75d leads (lags) Nadir-30y. Figure 8a shows that SWOT-75d has large point-wise phase anomalies, with a root-mean-square (RMS) value of 84°. The large phase anomalies are mainly errors, because SWOT-75d has amplitude errors about 5 mm, compared to 0.7 mm for Nadir-30y (Figure 4). Despite the large errors in phase, we can see obvious large-scale phase anomalies in many regions including the western North Pacific Ocean. The phase error e_ϕ can be roughly estimated from the amplitude error e_A and the wave amplitude A following the ratio

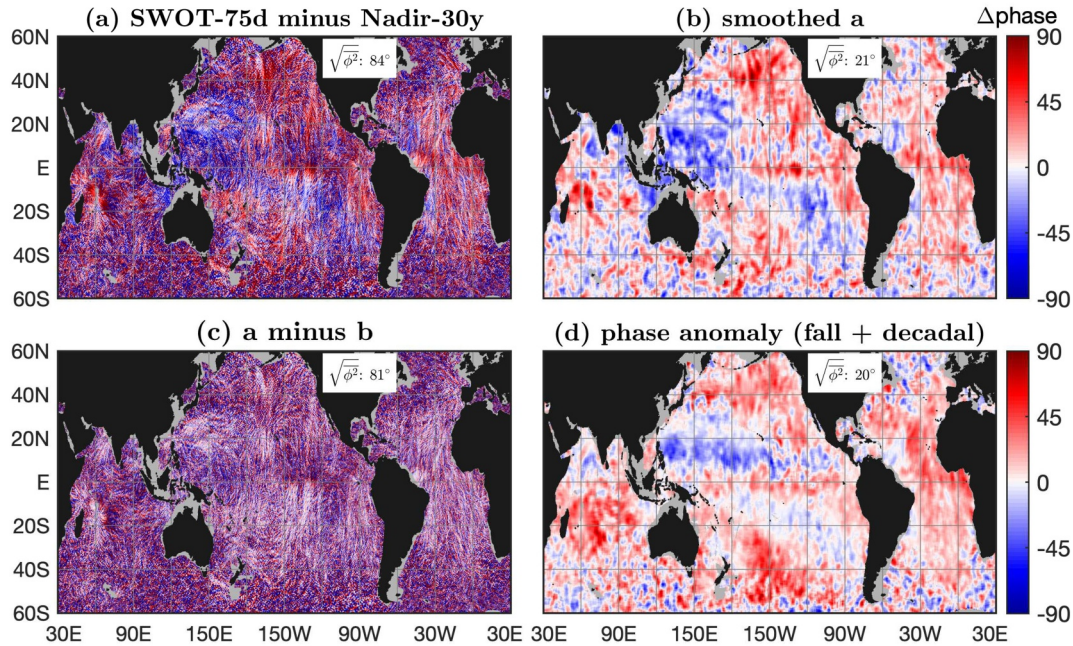

Figure 8. Phase anomaly of SWOT-75d with respect to Nadir-30y. (a) Point-wise difference. (b) 3° × 3° smoothed difference. (c) Residual. (d) Phase anomaly estimated using internal tides mapped by nadir altimetry (Appendix B).

e_A/A. For the same amplitude error, larger amplitudes lead to smaller phase errors. This explains why SWOT-75d has large phase errors in regions of weak internal tides and low phase errors in regions of strong internal tides (Figure 8a). We can suppress errors by spatial smoothing the point-wise phase anomalies and thus removing small-scale errors. In this study, we smooth the point-wise anomalies in 3° × 3° windows. Figure 8b shows the smoothed phase anomalies. Positive values appear in the Atlantic Ocean, the Northeast Pacific Ocean, and the Southwest Pacific Ocean. Negative values are observed in the western Pacific and the eastern Indian Ocean. The smoothed phase anomalies have an RMS value of 21°. For comparison, the residual phase anomalies have an RMS value of 81°, suggesting that most of the point-wise phase anomalies are small-scale variations (Figure 8c). Note that our simple spatial smoothing cannot fully suppress small-scale features, as Figure 8b still shows large phase errors in regions of weak internal tides such as the eastern tropical Pacific.

We find that the phase anomalies shown in Figure 8b are mainly caused by the temporal variations of M_2 internal tides over seasonal, interannual, and decadal timescales (Zhao, 2021, 2022a, 2023b). Appendix B describes our methods of calculating seasonal and decadal phase anomalies. Figure B1 shows that the seasonal and decadal phase anomalies have RMS values of 13° and 17°, respectively. Because SWOT-75d is constructed using data mainly in fall, we estimate the phase anomalies combining fall and decadal anomalies (Figure 8d). Figures 8b and 8d have similar spatial patterns. For example, both show positive phase anomalies in the Atlantic Ocean and negative values in the western North Pacific Ocean. Figures 8b and 8d have a tight correlation (correlation coefficient is 0.41) and close RMS values of 20° and 21°. The agreement suggests that the phase anomalies of SWOT-75d (Figure 8b) are mainly caused by seasonal and decadal variation of mode-1 M_2 internal tides. Note that Figures 8b and 8d have noticeable differences, which may be caused by the year-to-year variation, because Figure 8b gives instantaneous phase anomalies and Figure 8d gives only the seasonal and decadal phase anomalies.

In conclusion, we find that SWOT-75d and Nadir-30y have large systematic phase anomalies, which are mainly caused by the seasonal and decadal variations of internal tides. The large phase anomalies imply that Nadir-30y cannot correct the time-varying internal tides in SWOT. In the next section, we will show that the large phase anomalies can be used to better correct internal tides for SWOT.

5.2. A Phase-Adjusted Internal Tide Model

In this study, we bring up a new method of internal tide correction for SWOT. We construct an internal tide model Nadir-30y* from Nadir-30y. The two models have the same amplitudes. But the phases in Nadir-30y* are

adjusted by the smoothed phase anomalies of SWOT-75d (Figure 8b). Specifically, the phases in Nadir-30y* are adjusted following

$$\phi^{\star}_{30y} = \phi_{30y} + \overline{\overline{\phi_{75d} - \phi_{30y}}}, \tag{2}$$

where $\phi^{\star}_{30y}$, ϕ_{30y}, and ϕ_{75d} are phases in Nadir-30y*, Nadir-30y, and SWOT-75d, respectively, and the overlines indicate 3° by 3° spatial smoothing in both directions. We have tested five smoothing windows from 1° to 5° and found no significant differences. By adjusting the phases in Nadir-30y*, we actually take into account the instantaneous phases during 7 September to 21 November 2023. Therefore, we expect that Nadir-30y* can better correct internal tides in the SWOT data. Note that our phase adjustment is using the smoothed phase anomalies (Figure 8b), instead of the point-wise phase anomalies (Figure 8a). In fact, a phase adjustment using the latter is equivalent to using the phase in SWOT-75d and thus the phases of Nadir-30y* are not independent of the SWOT data. Note that SWOT-75d has large amplitude errors of 5 mm, so that we cannot detect and correct seasonal and decadal changes in amplitude. By this method, we can partially correct incoherent internal tides in SWOT.

5.3. Application to the SWOT Data

We next evaluate Nadir-30y and Nadir-30y* using the 75 days of SWOT data from 7 September to 21 November 2023, the same data for constructing SWOT-75d (Figures 1 and 2). We predict internal tides using the two models and subtract them from the 75 days of SWOT data following the same procedure (Section 4.3). Figure 9a shows the resulting 1° by 1° binned variance reductions. Figures 9a and 9b show variance reductions caused by Nadir-30y and Nadir-30y*, respectively. The model improvement is indicated by their differences as shown in Figure 9c. Both models cause positive variance reductions throughout the global ocean, suggesting that both models can make internal tide correction for SWOT. Figure 9c shows that their differences are dominantly positive, suggesting that Nadir-30y* can reduce more variance. Quantitatively, their area-weighted mean variance reductions are 16.0 and 19.3 mm^2, respectively. It means that Nadir-30y* can reduce 3.3 mm^2 more variance than Nadir-30y by adjusting phases. It is equivalent to a 20% improvement in model performance. It is because Nadir-30y* contains instantaneous phases, but Nadir-30y contains phases estimated from past observations.

5.4. Application to Nadir Altimetry Data

We next evaluate Nadir-30y and Nadir-30y* using the full-year nadir altimetry data in 2023. The resulting variance reductions are shown in Figures 9d and 9e. We find that their area-weighted mean variance reductions are 16.3 and 16.4 mm^2, respectively, suggesting that Nadir-30y and Nadir-30y* have similar performances. Their variance reduction differences (Figure 9f) suggest that their performances are a function of location. Nadir-30y* performs better in regions such as the central North Pacific Ocean, the Melanesian region, the central South Pacific Ocean, and the tropical South Atlantic Ocean, where significant decadal phase anomalies are observed (Figure B1e). Nadir-30y performs better in the tropical zone including the Madagascar–Mascarene region, the Indonesian Seas, the western North Pacific Ocean, and the Amazon shelf, where significant seasonal phase anomalies are observed (Figures B1a–B1d). The contrast indicates that the internal tide correction is affected both by the seasonal and decadal phase anomalies.

We further evaluate Nadir-30y and Nadir-30y* using four seasonal subsets of the nadir altimetry data in 2023. The variance reductions caused by Nadir-30y have been shown in Figures 6e–6h. Those caused by Nadir-30y* are very similar (not shown). Our research interest is to examine their differences, which represent the variance reduction changes with the phase adjustment. Figure 10 shows the variance reduction differences of Nadir-30y* minus Nadir-30y. It shows that the impact is different for the four seasons. On a global scale, the phase adjustment improves the correction in summer and fall, but worsens it in winter and spring. Among them, the best improvement is in fall. The improvement is 2.5 mm^2 over 14.7 mm^2 caused by Nadir-30y (Figure 6h), which is equivalent to an improvement by 17%.

Figure 10 demonstrates a remarkable spatial pattern. In all four seasons, the phase adjustment improves the correction in the following regions: the tropical South Atlantic Ocean, the central North Pacific Ocean, the Melanesian region, and the central South Pacific Ocean. The first three regions are where SWOT-75d performs better than Nadir-30y (Figure 7), because SWOT-75d contains instantaneous phases. The central South Pacific

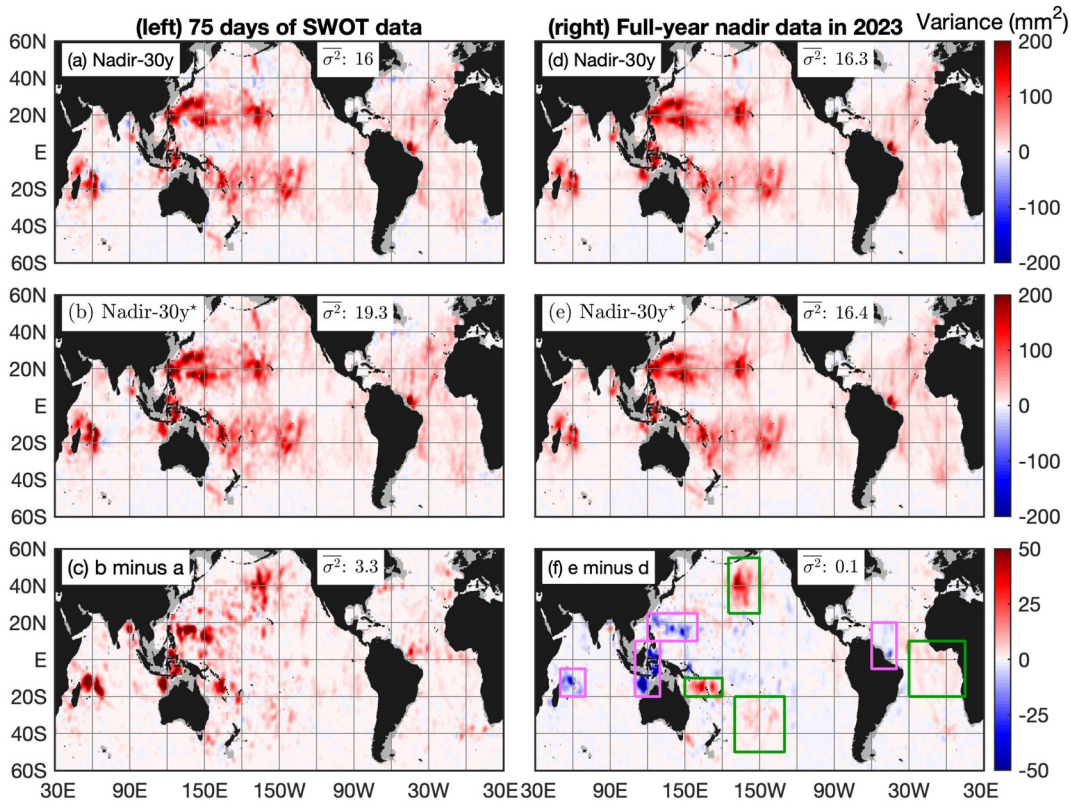

Figure 9. Evaluation of Nadir-30y and Nadir-30y* using 75 days of SWOT data (left) and nadir altimetry data in 2023 (right). Shown are variance reductions obtained by making internal tide correction. (a, d) Nadir-30y. (b, e) Nadir-30y*. (c, f) Differences. Global area-weighted mean values are given. Nadir-30y and Nadir-30y* have opposite performances in green and magenta boxes.

Ocean is subject to the largest decadal phase anomalies (Zhao, 2023b). This feature suggests that the reduction differences are not caused by seasonal variability, but by decadal variability. It is consistent with the decadal phase change shown in Figure B1e, where we find that all these four regions changed with global ocean warming.

In the tropical zone, the performance has a seasonal cycle. In winter and spring, the phase adjustment worsens the correction in all the regions. In summer, the phase adjustment worsens the correction in the Indian Ocean and western Pacific Ocean. In fall, the phase adjustment improves the performance throughout the tropical zone. All these features are consistent with the seasonal phase variation. In other words, there is strong seasonal phase variation in tropical zones. The phase adjustment in fall makes an improvement in fall, but may worsen other seasons. We thus conclude that the instantaneous phases can be used to their own time windows (i.e., fall in this study).

6. Impact of the 1-Day Repeat Data

The SWOT project also published 103 days of SWOT data along its 1-day repeat orbit from 29 March to 10 July 2023 (Figure 1, red bar). The 1-day repeat data are along 28 swaths only (Figure 2, red line); therefore, we cannot extract mode-1 M_2 internal tides by our mapping technique. To examine the impact of the 1-day repeat data, we instead map mode-1 M_2 internal tides by merging the 1-day and 21-day repeat data. We obtain an M_2 internal tide model following the same mapping procedure using the same mapping parameters (Section 3), regardless of the spatial inhomogeneity of the merged data. The model is labeled SWOT-178d. We evaluate SWOT-178d using the same full-year nadir altimetry data in 2023 (Section 4.3). Figure 11 shows the two models and their differences in amplitude, variance reduction, error, and phase. For amplitude, error, and phase, we first calculate their differences point by point and then smooth the differences in 2° by 2° windows. For variance reduction, we smooth the point-wise differences by 2-D three-point running mean. Figure 11 shows

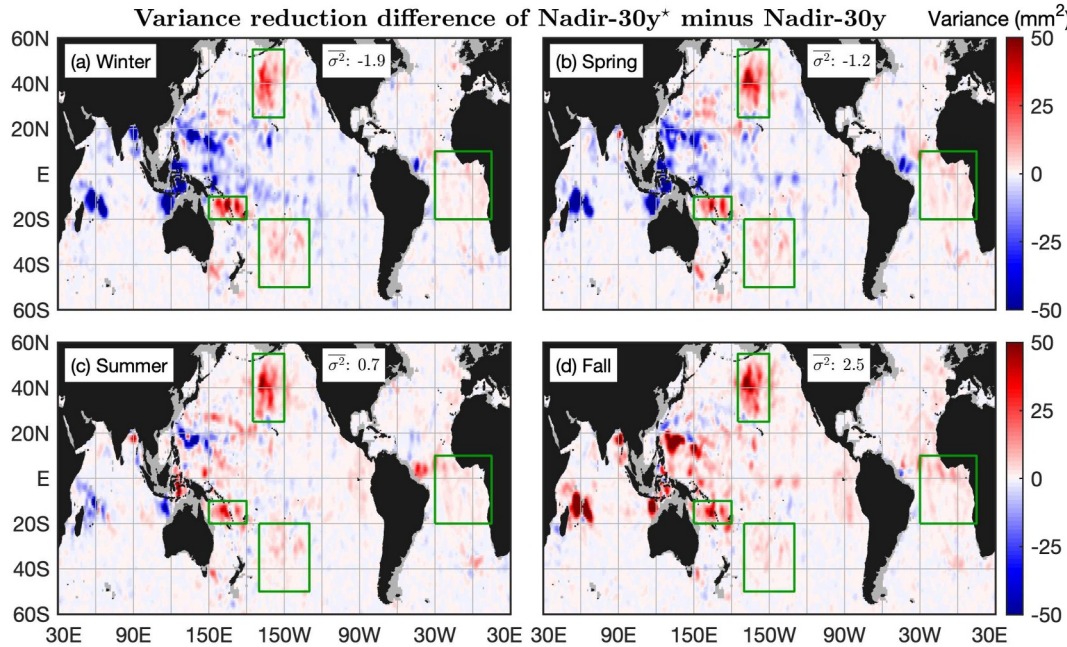

Figure 10. Evaluation of Nadir-30y and Nadir-30y* using four seasonal subsets of the nadir altimetry data in 2023. (a) Winter (JFM). (b) Spring (AMJ). (c) Summer (JAS). (d) Fall (OND). Global area-weighted mean values are given. Large differences are highlighted by green boxes.

that SWOT-178d and SWOT-75d have similar spatial patterns, with a correlation coefficient of 0.93. Off the 1-day orbit, SWOT-178d and SWOT-75d are almost the same for all variables (amplitude, variance reduction, error, and phase). It is because SWOT-178d and SWOT-75d off the 1-day orbit are constructed using the same SWOT data (Figure 2). This feature means that the addition of the 1-day repeat data does not affect the internal tide solution off the 1-day orbit.

Along the 1-day orbit, however, SWOT-178d and SWOT-75d are different, as a result of the addition of the 1-day repeat data. SWOT-178d has lower amplitudes (Figure 11c), but it can reduce more variance in the independent altimetry data (Figure 11d). This feature suggests that the decrease in amplitude is mainly due to the decrease in model errors. To examine this point, we estimate model errors in SWOT-178d following the same method as described in Section 4.2. The result shows that SWOT-178d has much lower model errors (Figure 11e). It is reasonable that a longer data record leads to lower model errors. Specifically, the mean error along the 1-day orbit in SWOT-178d is 2.5 mm, about half of that in SWOT-75d (Figure 4a). The result shows that the addition of the 1-day repeat data leads to a better internal tide model.

Figure 11f shows that SWOT-178d and SWOT-75d have large phase differences along the 1-day orbit. We suggest that the differences are mainly due to the seasonal phase differences in spring and fall. SWOT-75d is constructed using data in September–November. In contrast, the SWOT data along the 1-day orbit in SWOT-178d are dominantly from 29 March to 10 July 2023 (Figure 1, red bar). Figure B1 shows that M_2 internal tides have different spatial patterns in spring and fall. We calculate the phase differences between spring and fall, and obtain a similar spatial pattern (not shown) as in Figure 11f. We conclude that the phase differences between SWOT-178d and SWOT-75d stem mainly from the seasonal phase variability.

7. Summary and Perspectives

In this paper, we mapped and studied the global mode-1 M_2 internal tides using 75 days of SWOT data from 7 September to 21 November 2023. We also constructed another model Nadir-30y using 30 years of nadir altimetry data from 1993 to 2022. Despite its large errors, SWOT-75d reveals the basic features of the global mode-1 M_2 internal tide field. Evaluation using the full-year nadir altimetry data in 2023 revealed that SWOT-75d reduces variance in regions of strong internal tides. In particular, SWOT-75d performs better than Nadir-30y in regions including the tropical South Atlantic Ocean, the central North Pacific Ocean, and the Melanesian region.

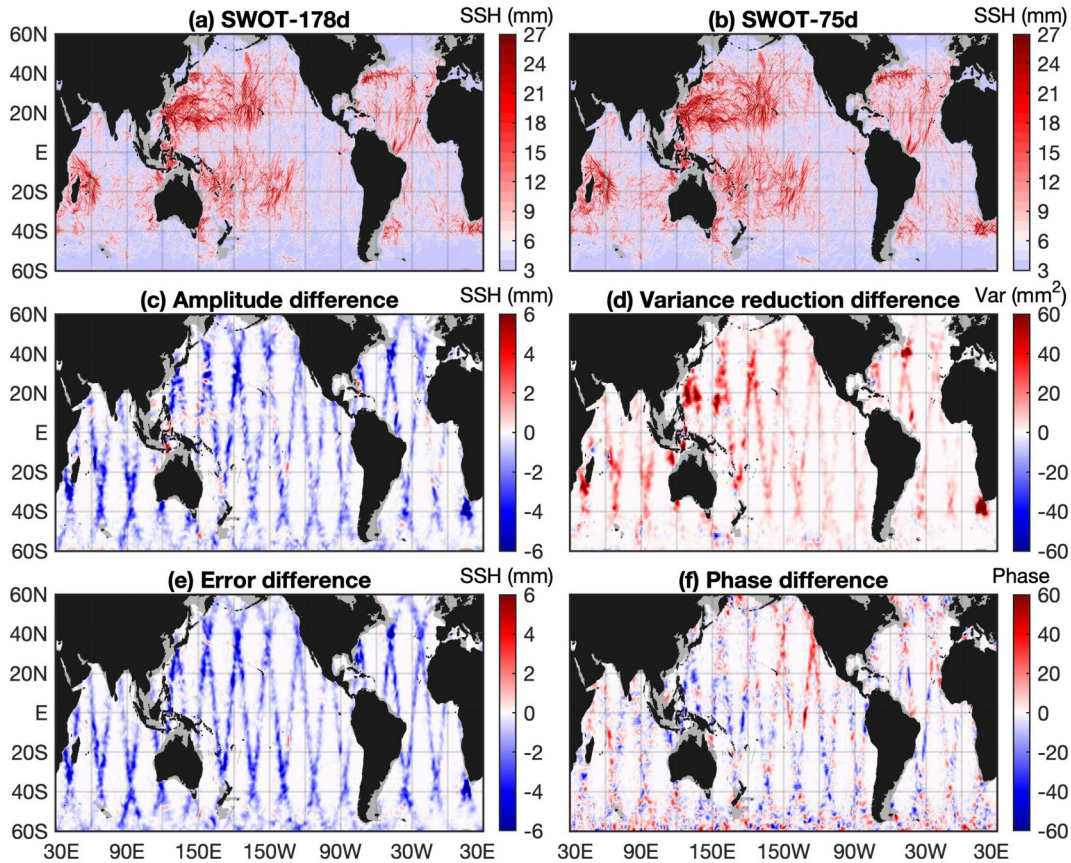

Figure 11. Comparison of SWOT-178d and SWOT-75d. (a) SWOT-178d. (b) SWOT-75d. (c–f) Differences of SWOT-178d minus SWOT-75d. (c) Amplitude. (d) Variance reduction to the full-year nadir altimetry data in 2023. (e) Error. (f) Phase.

Evaluation using seasonal subsets of the nadir altimetry data in 2023 showed that SWOT-75d performs the best in fall, because the model itself is constructed using SWOT data largely in fall. Our results demonstrated that we can map mode-1 M_2 internal tides using 75 days of SWOT data by our mapping technique.

We investigated the impact of the 1-day repeat data. To this end, we constructed an internal tide model using the merged 1-day and 21-day data. Off the 1-day orbit, the internal tide model is not affected by the addition of the 1-day data. Along the 1-day orbit, the internal tide model is greatly improved. Our results suggested that the SWOT derived internal tide model will improve with increasing SWOT data record in the coming years. SWOT entered its science phase in July 2023 and has been monitoring the global ocean since. We anticipate that better and better internal tide models will be constructed with more and more SWOT data becoming available. Our work demonstrated that SWOT greatly improves our capability of observing internal tides on a global scale.

We showed that SWOT-75d has large phase anomalies with respect to Nadir-30y. Nadir-30y represents the climate normal of internal tides averaged over 30 years from 1993 to 2022. SWOT-75d represents the instantaneous M_2 internal tide model in September–November 2023. The phase anomalies are mainly caused by the temporal variations of internal tides over seasonal, interannual, and decadal timescales. We brought up a method for better correcting internal tides for SWOT. We adjusted the phases in Nadir-30y using the spatially smoothed phase anomalies of SWOT-75d. We found that the phase adjustment improves the model performance by 20% for SWOT, mainly because the phase-adjusted model can partly correct the time-varying internal tides in SWOT.

It is well known in the community that it is a challenging task to correct incoherent internal tides for SWOT (Carrere et al., 2021). However, this task is a key step for SWOT to detect submesoscale motions (Fu et al., 2024; Morrow et al., 2019). All previous empirical internal tide models are constructed using satellite altimetry data

spanning over many years and thus cannot correct the time-varying internal tides in SWOT. In this work, we constructed a 75-day instantaneous internal tide model and derived its phase anomalies with respect to Nadir-30y. We showed that the phase anomalies caused internal tide variations over seasonal, interannual, and decadal timescales (Zaron & Egbert, 2014; Zhao, 2016, 2023b). We found that the large phase anomalies can be used to correct the time-varying internal tides in the SWOT data. We thus concluded that the phases in the SWOT-derived internal tide models can be used to improve internal tide correction for SWOT. Our new method has the following advantage: It is based on an analysis of the SWOT data, and does not require data from other observational platforms. This finding has important implications for making internal tide correction for SWOT.

Appendix A: Empirical Cutoff Wavenumbers

Our mapping procedure comprises a spatial 2-D bandpass filter in the second step (Section 3.2). It utilizes the local theoretical wavenumber of mode-1 M_2 internal tides calculated from the WOA18 hydrography. In our previous studies, the bandpass filter width is empirically chosen to be (0.8, 1.25) times the local wavenumber (for Nadir-30y). However, the SWOT data in this study are only 75 days long. For such a short data record, our previous bandpass width seems a little wider. Here we empirically determine the bandpass width for the SWOT data. We examine the low and high cutoff wavenumbers separately. For the low cutoff wavenumber, we test seven values from 0.65 to 0.95 with a step of 0.05. For the high cutoff wavenumber, we test seven values from 0.95 to 1.35 with a step of 0.05. All other parameters are kept the same. We thus obtain 14 internal tide models. We evaluate the models using the full-year nadir altimetry data in 2023. Figure A1 shows the area-weighted mean variance reductions explained by the 14 models. We chose the bandpass width of (0.9, 1.2), because it gives the largest variance reduction. Since Nadir-75d and Nadir-30y are constructed using different bandpass widths, it is meaningless to compare their amplitudes. In fact, their amplitude differences are dominated by model errors (Figure 4).

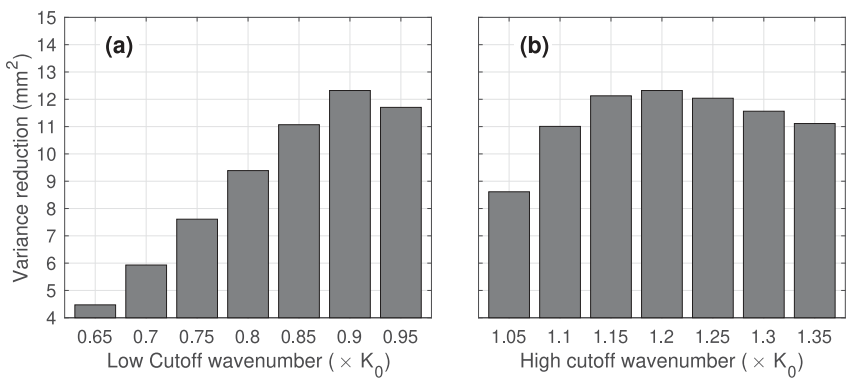

Figure A1. Determination of cutoff wavenumbers in spatial bandpass filtering. Shown are variance reductions obtained by making internal tide correction to the full-year nadir altimetry data in 2023. (a) Low cutoff wavenumber. (b) High cutoff wavenumber. A bandpass width of (0.9, 1.2) is chosen.

Appendix B: Seasonal and Decadal Phase Anomalies

In Zhao (2021), we investigated the seasonal variability of mode-1 M_2 internal tides using 25 years of satellite altimetry data from 1993 to 2017. We constructed four seasonal mode-1 M_2 models using seasonally subsetted altimeter data and seasonal hydrography in the WOA13. We recently updated Zhao (2021) using 30 years of satellite altimetry data from 1993 to 2022 and seasonal hydrography in the WOA18 by our new mapping technique described in Section 3.3 (unpublished). We found that mode-1 M_2 internal tides are subject to significant seasonal variations in both amplitude and phase. Figure B1 shows seasonal phase anomalies with respect to Nadir-30y. We found large phase anomalies in all four seasons, with RMS anomalies of about 13°. Figure B1 reveals the following remarkable features. Large seasonal phase anomalies mainly occur in the tropical zone. The opposite seasons (or southern and northern hemispheres) have opposite phase anomalies. The largest seasonal phase anomalies occur in the Arabian Sea. The seasonal phase anomalies have been validated using independent altimetry data (Zhao, 2021). Meanwhile, we have calculated the speeds of mode-1 M_2 internal tides in the four seasons using the WOA18. We found that the seasonal speed anomalies and the seasonal phase anomalies have similar spatial patterns (Zhao, 2021, Figure 1), suggesting that the seasonal phase anomalies are caused by the seasonal speed anomalies. In this study, we demonstrate that the seasonal phase anomalies affect the model performance.

In Zhao (2023b), we investigated the decadal changes of mode-1 M_2 internal tides using 30 years of altimetry data from 1993 to 2022. We constructed two mode-1 M_2 models M9509 and M1019 using divided data records in 1995–2009 and 2010–2019, respectively. The altimetry data in 1993–1994 and 2020–2022 were reserved for model evaluation. We found that mode-1 M_2 internal tides strengthened over the past 30 years (Zhao, 2023b). In addition, we found large phase anomalies between the two decades. On a global average, M1019 leads M9509 by

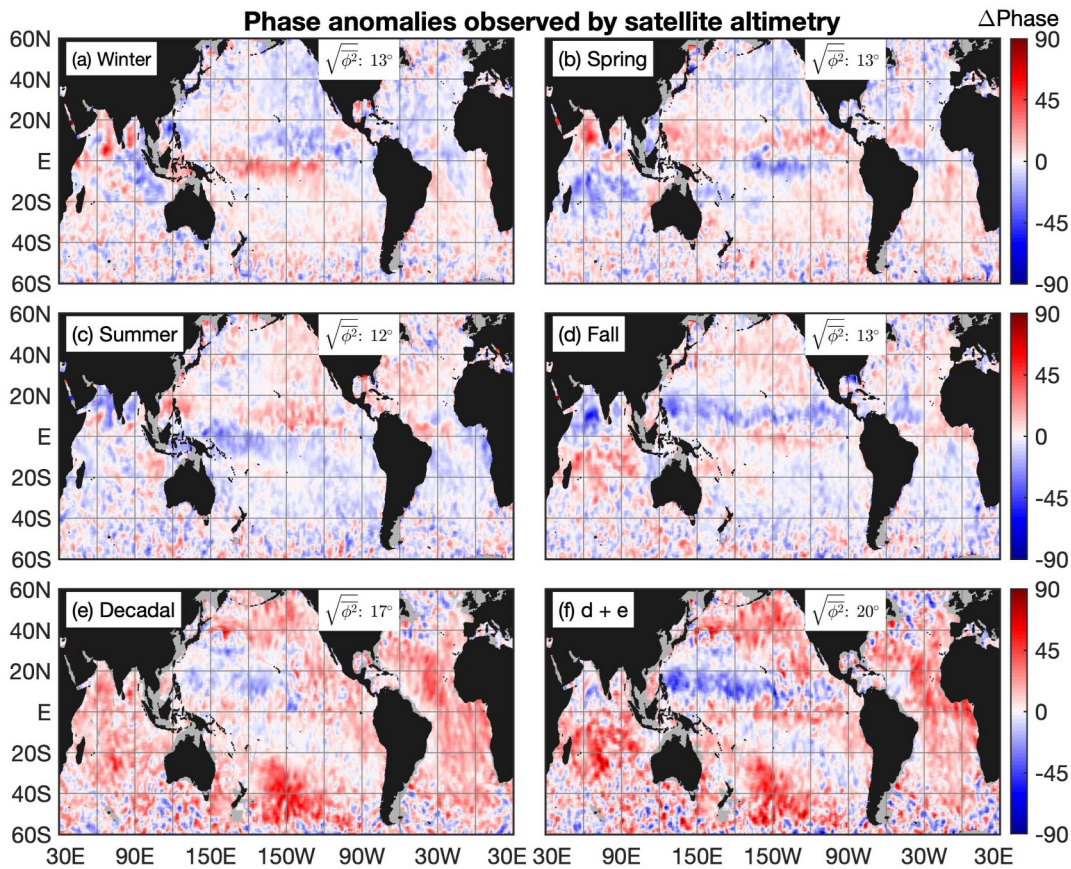

Figure B1. Seasonal and decadal phase anomalies of mode-1 M_2 internal tides. The seasonal phase anomalies are updated from Zhao (2021). The decadal phase anomalies are from Zhao (2023b). (a) Winter. (b) Spring. (c) Summer. (d) Fall. (e) Decadal (M1019 minus M9509). (f) Fall and decadal phase anomalies combined.

about 10° (20 min in time). Figure B1e shows the decadal phase anomalies. It shows that M1019 leads M9509 throughout the ocean, except for the western North Pacific Ocean. The RMS decadal phase anomaly is 17°. Note that the data-weighted central times of M9509 and M1019 are March 2003 and August 2015, respectively, with a time span of 12.5 years. For comparison, the data-weighted central times of Nadir-30y and SWT-75d are December 2011 and October 2023, respectively, with a time span of 11.8 years. Because the two time spans are very close, we estimate the phase anomalies between M1019 and M9509 using those between SWOT-75d and Nadir-30y. In this study, we demonstrate that the decadal phase anomalies affect the model performance.

Appendix C: Sensitivity Analysis: Separation of S_2, M_2, and N_2

One major concern is whether M_2 internal tides can be separated from S_2 and N_2 using 75 days of SWOT data. This concern is addressed here by a sensitivity analysis of the M_2 spectral peak. Specifically, we map 40 internal tide models in the semidiurnal band with periods ranging from 12 hr (S_2) to 12.6583 hr (N_2) with 1-min steps. They are extracted from the same 75-day SWOT data following the same mapping procedure but using their respective tidal periods and theoretical wavelengths. Limited by our computational capability. This analysis is conducted in a typical region around the Hawaiian Ridge (0–30°N, 180–150°W). Figure C1 shows six sample internal tide fields and our analysis results.

Six example internal tide models are shown in Figures C1a–C1f. They are three major constituents S_2, M_2, and N_2, and three background internal tides off major constituents. We find that S_2 (Figure C1a) and M_2 (Figure C1d) have larger amplitudes than background internal tides. Figure C1g shows the histogram of mean SSH amplitudes of the 40 internal tide models. It shows that the M_2 spectral peak (tidal cusp) is about 10 min wide (±5 min), far from S_2 (−25 min) to N_2 (+15 min). Similarly, the S_2 spectral peak is about 5 min wide on its right (half of its cusp). The weak N_2 internal tides are overwhelmed by errors and do not have a tidal cusp. We further calculate the correlation of M_2 and the 40 internal tide models and show their correlation coefficients in Figure C1h. Similarly, the correlation coefficients of S_2 and N_2 with the 40 internal tide models are shown in Figures C1i and C1j. It shows that the background internal tides outside the M_2 cusp have low correlation with M_2, suggesting that the M_2 spectral peak is about 10 min wide too. We thus conclude that M_2 internal tides can be separated from S_2 to N_2 using 75 days of SWOT data. In other words, our mode-1 M_2 model SWOT-75d contains no leaked signals from S_2 or N_2.

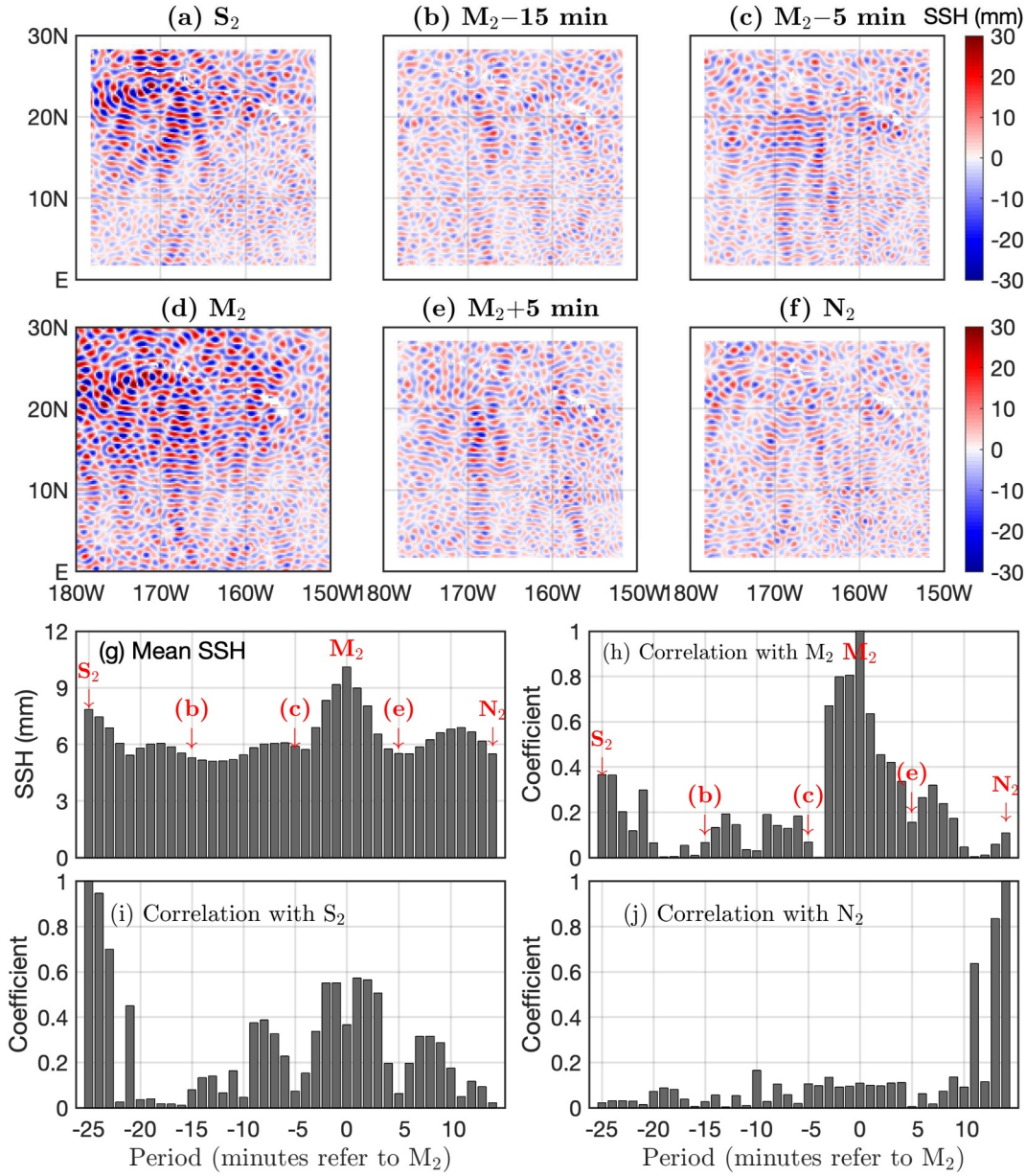

Figure C1. Forty internal tide models in the semidiurnal band with 1-min steps. They are mapped using the same 75-day SWOT data and following the same mapping procedure but using their respective tidal periods and theoretical wavelengths. (a) S_2. (b) M_2 minus 15 min (c) M_2 minus 5 min (d) M_2. (e) M_2 plus 5 min (f) N_2. (g) Histogram of mean SSH amplitudes. (h) Correlation with M_2. (i) Correlation with S_2. (h) Correlation with N_2. The result shows that M_2 contains no leaked S_2 or N_2 signals, because (a) the M_2 spectral peak (tidal cusp) is ±5 min wide, far from S_2 (−25 min) to N_2 (+15 min), and (b) the correlation coefficients of M_2 and other constituents are low outside its tidal cusp.

Data Availability Statement

The SWOT_L3_SSH product, derived from the L2 SWOT KaRIn Low rate ocean data products (NASA/JPL and CNES), is produced and made freely available by AVISO and DUACS teams as part of the DESMOS Science Team project. The SWOT data used in this paper are labeled "SWOT Level-3 SSH Expert (v0.3)" and downloaded from https://doi.org/10.24400/527896/A01-2023.018. The mode-1 M_2 internal tide models SWOT-75d, SWOT-178d, and Nadir-30y are accessible to the public (Zhao, 2024).

Acknowledgments
This work was supported by NSF OCE2149028. The author thanks two anonymous reviewers and Editor Mar Flexas for their constructive suggestions.

References

Alford, M. H. (2003). Redistribution of energy available for ocean mixing by long-range propagation of internal waves. *Nature*, *423*(6936), 159–162. https://doi.org/10.1038/nature01628

Arbic, B. K. (2022). Incorporating tides and internal gravity waves within global ocean general circulation models: A review. *Progress in Oceanography*, *206*, 102824. https://doi.org/10.1016/j.pocean.2022.102824

Boyer, T. P., García, H. E., Locarnini, R. A., Zweng, M. M., Mishonov, A. V., Reagan, J. R., et al. (2018). *World Ocean Atlas 2018*. NOAA National Centers for Environmental Information. Retrieved from https://www.ncei.noaa.gov/products/world-ocean-atlas

Carrere, L., Arbic, B. K., Dushaw, B., Egbert, G. D., Erofeeva, S. Y., Lyard, F., et al. (2021). Accuracy assessment of global internal tide models using satellite altimetry. *Ocean Science*, *17*(1), 147–180. https://doi.org/10.5194/os-17-147-2021

Dibarboure, G., Ubelmann, C., Flamant, B., Briol, F., Peral, E., Bracher, G., et al. (2022). Data-driven calibration algorithm and pre-launch performance simulations for the SWOT mission. *Remote Sensing*, *14*(23), 6070. https://doi.org/10.3390/rs14236070

Durand, M., Fu, L.-L., Lettenmaier, D. P., Alsdorf, D. E., Rodriguez, E., & Esteban-Fernandez, D. (2010). The Surface Water and Ocean Topography mission: Observing terrestrial surface water and oceanic submesoscale eddies. *Proceedings of the IEEE*, *98*(5), 766–779. https://doi.org/10.1109/JPROC.2010.2043031

Egbert, G. D., & Ray, R. D. (2000). Significant dissipation of tidal energy in the deep ocean inferred from satellite altimeter data. *Nature*, *405*(6788), 775–778. https://doi.org/10.1038/35015531

Fu, L.-L., & Ferrari, R. (2008). Observing oceanic submesoscale processes from space. *Eos, Transactions American Geophysical Union*, *89*(48), 488. https://doi.org/10.1029/2008EO480003

Fu, L.-L., Pavelsky, T., Cretaux, J.-F., Morrow, R., Farrar, J. T., Vaze, P., et al. (2024). The surface water and Ocean topography mission: A breakthrough in radar remote sensing of the ocean and land surface water. *Geophysical Research Letters*, *51*(4), e2023GL107652. https://doi.org/10.1029/2023GL107652

Garrett, C., & Kunze, E. (2007). Internal tide generation in the deep ocean. *Annual Review of Fluid Mechanics*, *39*(1), 57–87. https://doi.org/10.1146/annurev.fluid.39.050905.110227

Jayne, S. R., & St. Laurent, L. C. (2001). Parameterizing tidal dissipation over rough topography. *Geophysical Research Letters*, *28*(5), 811–814. https://doi.org/10.1029/2000GL012044

Kelly, S. M. (2016). The vertical mode decomposition of surface and internal tides in the presence of a free surface and arbitrary topography. *Journal of Physical Oceanography*, *46*(12), 3777–3788. https://doi.org/10.1175/JPO-D-16-0131.1

Kelly, S. M., Lermusiaux, P. F. J., Duda, T. F., & Haley, P. J. (2016). A coupled-mode shallow-water model for tidal analysis: Internal tide reflection and refraction by the Gulf Stream. *Journal of Physical Oceanography*, *46*(12), 3661–3679. https://doi.org/10.1175/JPO-D-16-0018.1

MacKinnon, J. A., Zhao, Z., Whalen, C. B., Waterhouse, A. F., Trossman, D. S., Sun, O. M., et al. (2017). Climate process team on internal wave-driven ocean mixing. *Bulletin of the American Meteorological Society*, *98*(11), 2429–2454. https://doi.org/10.1175/BAMS-D-16-0030.1

Masunaga, E., Arthur, R. S., & Yamazaki, H. (2020). Baroclinic residual circulation and mass transport due to internal tides. *Journal of Geophysical Research: Oceans*, *125*(4), e2019JC015316. https://doi.org/10.1029/2019JC015316

Melet, A., Legg, S., & Hallberg, R. (2016). Climatic impacts of parameterized local and remote tidal mixing. *Journal of Climate*, *29*(10), 3473–3500. https://doi.org/10.1175/JCLI-D-15-0153.1

Morrow, R., Fu, L.-L., Ardhuin, F., Benkiran, M., Chapron, B., Cosme, E., et al. (2019). Global observations of fine-scale ocean surface topography with the Surface Water and Ocean Topography (SWOT) mission. *Frontiers in Marine Science*, *6*, 232. https://doi.org/10.3389/fmars.2019.00232

Munk, W. H., & Wunsch, C. (1998). Abyssal recipes II: Energetics of tidal and wind mixing. *Deep-Sea Research I*, *45*(12), 1977–2010. https://doi.org/10.1016/S0967-0637(98)00070-3

Nash, J. D., Kelly, S. M., Shroyer, E. L., Moum, J. N., & Duda, T. F. (2012). The unpredictable nature of internal tides on continental shelves. *Journal of Physical Oceanography*, *42*(11), 1981–2000. https://doi.org/10.1175/JPO-D-12-028.1

Pujol, M.-I., Faugère, Y., Taburet, G., Dupuy, S., Pelloquin, C., Ablain, M., & Picot, N. (2016). DUACS DT2014: The new multi-mission altimeter data set reprocessed over 20 years. *Ocean Science*, *12*(5), 1067–1090. https://doi.org/10.5194/os-12-1067-2016

Qiu, B., Chen, S., Wang, J., & Fu, L.-L. (2024). Seasonal and fortnight variations in internal solitary waves in the Indonesian Seas from the SWOT measurements. *Journal of Geophysical Research: Oceans*, *129*(7), e2024JC021086. https://doi.org/10.1029/2024JC021086

Ray, R. D., & Mitchum, G. T. (1996). Surface manifestation of internal tides generated near Hawaii. *Geophysical Research Letters*, *23*(16), 2101–2104. https://doi.org/10.1029/96GL02050

Ray, R. D., & Mitchum, G. T. (1997). Surface manifestation of internal tides in the deep ocean: Observations from altimetry and island gauges. *Progress in Oceanography*, *40*(1), 135–162. https://doi.org/10.1016/S0079-6611(97)00025-6

Ray, R. D., & Susanto, R. D. (2016). Tidal mixing signatures in the Indonesian Seas from high-resolution sea surface temperature data. *Geophysical Research Letters*, *43*(15), 8115–8123. https://doi.org/10.1002/2016GL069485

Ray, R. D., & Zaron, E. (2016). M_2 internal tides and their observed wavenumber spectra from satellite altimetry. *Journal of Physical Oceanography*, *46*(1), 3–22. https://doi.org/10.1175/JPO-D-15-0065.1

Rodriguez, E., Esteban-Fernandez, D., Peral, E., Chen, C., De Bleser, J., & Williams, B. (2017). Wide-swath altimetry: A review. In D. Stammer & A. Cazenave (Eds.), *Earth observation of global changes* (pp. 71–112). CRC Press. https://doi.org/10.1201/9781315151779-2

Soares, S. M., Gille, S. T., Chereskin, T. K., Firing, E., Hummon, J., & Rocha, C. B. (2022). Transition from balanced to unbalanced motion in the eastern tropical pacific. *Journal of Physical Oceanography*, *52*(8), 1775–1795. https://doi.org/10.1175/JPO-D-21-0139.1

Spingys, C. P., Williams, R. G., Hopkins, J. E., Hall, R. A., Green, J. A. M., & Sharples, J. (2020). Internal tide-driven tracer transport across the continental slope. *Journal of Geophysical Research: Oceans*, *125*(9), e2019JC015530. https://doi.org/10.1029/2019JC015530

Storlazzi, C. D., Cheriton, O. M., van Hooidonk, R., Zhao, Z., & Brainard, R. (2020). Internal tides can provide thermal Refugia that will buffer some coral reefs from future global warming. *Scientific Reports*, *10*(1), 13435. https://doi.org/10.1038/s41598-020-70372-9

Susanto, R. D., & Ray, R. D. (2022). Seasonal and interannual variability of tidal mixing signatures in Indonesian seas from high-resolution sea surface temperature. *Remote Sensing*, *14*(8), 1934. https://doi.org/10.3390/rs14081934

SWOT Project. (2024). SWOT level-3 KaRIn low rate SSH Expert (v0.3) [Dataset]. *CNES*. https://doi.org/10.24400/527896/A01-2023.018

Taburet, G., Sanchez-Roman, A., Ballarotta, M., Pujol, M.-I., Legeais, J.-F., Fournier, F., et al. (2019). Duacs DT2018: 25 years of reprocessed sea level altimetry products. *Ocean Science*, *15*(5), 1207–1224. https://doi.org/10.5194/os-15-1207-2019

Torres, H. S., Klein, P., Menemenlis, D., Qiu, B., Su, Z., Wang, J., et al. (2018). Partitioning ocean motions into balanced motions and internal gravity waves: A modeling study in anticipation of future space missions. *Journal of Geophysical Research: Oceans*, *123*(11), 8084–8105. https://doi.org/10.1029/2018JC014438

Tuerena, R. E., Williams, R. G., Mahaffey, C., Vic, C., Green, J. A. M., Naveira-Garabato, A., et al. (2019). Internal tides drive nutrient fluxes into the deep chlorophyll maximum over mid-ocean ridges. *Global Biogeochemical Cycles*, *33*(8), 995–1009. https://doi.org/10.1029/2019GB006214

Ubelmann, C., Carrere, L., Durand, C., Dibarboure, G., Faugère, Y., Ballarotta, M., et al. (2022). Simultaneous estimation of ocean mesoscale and coherent internal tide sea surface height signatures from the global altimetry record. *Ocean Science*, *18*(2), 469–481. https://doi.org/10.5194/os-18-469-2022

Wang, J., Fu, L.-L., Torres, H. S., Chen, S., Qiu, B., & Menemenlis, D. (2019). On the spatial scales to be resolved by the surface water and ocean topography Ka-band radar interferometer. *Journal of Atmospheric and Oceanic Technology*, *36*(1), 87–99. https://doi.org/10.1175/JTECH-D-18-0119.1

Whalen, C. B., de Lavergne, C., Naveira Garabato, A. C., Klymak, J. M., MacKinnon, J. A., & Sheen, K. L. (2020). Internal wave-driven mixing: Governing processes and consequences for climate. *Nature Reviews Earth & Environment*, *1*, 606–621. https://doi.org/10.1038/s43017-020-0097-z

Zaron, E. D. (2019). Baroclinic tidal sea level from exact-repeating mission altimetry. *Journal of Physical Oceanography*, *49*(1), 193–210. https://doi.org/10.1175/JPO-D-18-0127.1

Zaron, E. D., Capuano, T. A., & Koch-Larrouy, A. (2023). Fortnightly variability of chl a in the Indonesian Seas. *Ocean Science*, *19*(1), 43–55. https://doi.org/10.5194/os-19-43-2023

Zaron, E. D., & Egbert, G. D. (2014). Time-variable refraction of the internal tide at the Hawaiian Ridge. *Journal of Physical Oceanography*, *44*(2), 538–557. https://doi.org/10.1175/JPO-D-12-0238.1

Zaron, E. D., & Elipot, S. (2024). Estimates of baroclinic tidal sea level and currents from Lagrangian drifters and satellite altimetry. *Journal of Atmospheric and Oceanic Technology*, *41*(8), 781–802. https://doi.org/10.1175/JTECH-D-23-0159.1

Zhang, W. G., Cheng, Z., & Ashton, A. D. (2021). Exploring the potential for internal tides to reshape the continental shelf edge seafloor. *Progress in Oceanography*, *195*, 102575. https://doi.org/10.1016/j.pocean.2021.102575

Zhao, Z. (2016). Internal tide oceanic tomography. *Geophysical Research Letters*, *43*(17), 9157–9164. https://doi.org/10.1002/2016GL070567

Zhao, Z. (2020). Southward internal tides in the Northeastern South China sea. *Journal of Geophysical Research: Oceans*, *125*(11), e2020JC01654. https://doi.org/10.1029/2020JC016554

Zhao, Z. (2021). Seasonal mode-1 M_2 internal tides from satellite altimetry. *Journal of Physical Oceanography*, *51*, 3015–3035. https://doi.org/10.1175/JPO-D-21-0001.1

Zhao, Z. (2022a). Development of the yearly mode-1 M_2 internal tide model in 2019. *Journal of Atmospheric and Oceanic Technology*, *39*(4), 463–478. https://doi.org/10.1175/JTECH-D-21-0116.1

Zhao, Z. (2022b). Satellite estimates of mode-1 M_2 internal tides using nonrepeat altimetry missions. *Journal of Physical Oceanography*, *52*(12), 3065–3076. https://doi.org/10.1175/JPO-D-21-0287.1

Zhao, Z. (2023a). Mode-1 N_2 internal tides observed by satellite altimetry. *Ocean Science*, *19*(4), 1067–1082. https://doi.org/10.5194/os-19-1067-2023

Zhao, Z. (2023b). Satellite evidence for strengthened M_2 internal tides in the past 30 years. *Geophysical Research Letters*, *50*(24), e2023GL105764. https://doi.org/10.1029/2023GL105764

Zhao, Z. (2024). An instantaneous M_2 internal tide model from SWOT [Dataset]. *figshare*. https://doi.org/10.6084/M9.FIGSHARE.27932304.V1

Zhao, Z., & Alford, M. H. (2009). New Altimetric estimates of mode-1 M_2 internal tides in the central North Pacific Ocean. *Journal of Physical Oceanography*, *39*(7), 1669–1684. https://doi.org/10.1175/2009JPO3922.1

Zhao, Z., Alford, M. H., Girton, J. B., Rainville, L., & Simmons, H. L. (2016). Global observations of open-ocean mode-1 M_2 internal tides. *Journal of Physical Oceanography*, *46*(6), 1657–1684. https://doi.org/10.1175/JPO-D-15-0105.1